Tuning structural, optical, and gas sensing properties of ceria-based materials by rare-earth doping

P.P. Ortega [a,*], B. Hangai [a], H. Moreno [a], L.S.R. Rocha [b], M.A. Ramírez [a], M.A. Ponce [c], E. Longo [b], A.Z. Simões [a]

[a] *São Paulo State University (UNESP) – School of Engineering of Guaratinguetá, Av. Dr. Ariberto Pereira da Cunha 333, Portal das Colinas, 12.516-410, Guaratinguetá, São Paulo, Brazil*
[b] *Federal University of São Carlos (UFSCar), Department of Chemistry, 13565-905 São Carlos, SP, Brazil*
[c] *University of Mar del Plata (UNMdP), Institute of Materials Science and Technology (INTEMA), National Research Council (CONICET), Av. Juan B. Justo 4302, 7600 Mar del Plata, Argentina*

A R T I C L E   I N F O

A B S T R A C T

In this study, we investigate the influence of rare-earth dopants on the structural, optical, gas sensing properties of $Ce_{1-(3/4)x}RE_xO_2$ (RE = Eu, La; x = 0.0 and 0.08) nanoparticles synthesized using the microwave-assisted hydrothermal method. X-ray diffraction analysis confirmed the formation of CeO_2 fluorite structure free of secondary phases. Raman spectroscopy indicates oxygen vacancies are the dominant defect in the samples. Additionally, doping with La and Eu decreased the bandgap energy of the pure sample. The different dopants changed the photoluminescence spectrum of pure ceria, leading to blue (La) and red (Eu) emissions with a higher number of electronic transitions for the Eu-doped nanoparticles, which consists of six bands between 550 and 750 nm. For the thick films fabricated using the as-prepared nanoparticles, a measurable response in terms of resistivity was observed during interactions with vacuum, dry air, and carbon monoxide atmospheres. The Eu-doped thick film reacted much faster (1 s) with carbon monoxide compared to La-doped (4.2 s) and pure ceria (6.6 s), corresponding to an improvement when compared with other studies reported in the literature. Doping the ceria structure proved to be beneficial to its carbon monoxide sensing properties and produced tunable photoluminescent emissions, which are promising for white LED applications.

© 2021 Elsevier B.V. All rights reserved.

1. Introduction

Over the last few years, the number of publications regarding cerium dioxide-based materials has experienced a boost. The growing interest in this compound is due to its unique properties and multifunctional characteristics. Cerium dioxide (CeO_2 or ceria) is an n-type semiconductor that crystallizes in a cubic fluorite structure, in which cerium and oxygen atoms occupy tetrahedral and octahedral sites, respectively. Ceria exhibits a reversible transition between Ce^{4+} and Ce^{3+} states, which creates or eliminates oxygen vacancies (V_o) to compensate for their charge difference, resulting in an oxygen non-stoichiometry (CeO_{2-x}) [1]. Upon reduction from Ce^{4+} to Ce^{3+}, two electrons previously localized in the O 2p states move to empty Ce 4f states near the oxygen vacancy [2]. The partially filled Ce 4f narrows the bandgap and favors oxygen mobility within the lattice. Doping the ceria structure with lower oxidation state cations leads to a higher concentration of oxygen vacancies, as elucidated by the Kroger-Vink notation in Eq. (1):

$$RE_2O_3 + CeO_2 \rightarrow Ce_{Ce}^x + 2RE_{Ce}' + 4O_O^x + V_O^{\cdot\cdot} + \tfrac{1}{2}O_{2(g)} \tag{1}$$
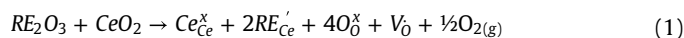
where RE_{Ce}' represents the substitution of Ce^{4+} by a RE^{3+} cation (RE = Eu^{3+}, La^{3+}, Sm^{3+}, etc.) with a negative effective charge, generating an oxygen vacancy ($V_O^{\cdot\cdot}$) to sustain charge neutrality. This process enhances oxygen mobility within the lattice, originating ceria capacity to release or uptake oxygen atoms (known as oxygen storage capacity) [3]. Therefore, doping is expected to improve ceria ionic conductivity and oxygen storage capacity. The possibility to exist in a partially reduced state makes ceria attractive for multiple applications, such as solid oxide fuel cells [4], white LEDs [5], magnetic hyperthermia [6], catalysis [7], and gas sensors [8].

Different elements have been used as ceria dopants, and their optical, magnetic, and photocatalytic properties have been investigated [9–12]. Balamurugan et al. [13] studied the effect of

---

samarium doping in the antibacterial activity of CeO_2. They observed that the Sm-doped samples performed better than pure ceria against *B. cereus* and ascribed the result to a higher oxygen vacancy concentration in the doped sample. Cheng et al. [14] synthesized RE-doped ceria (RE = La, Nd, Yb) particles for the chemical mechanical polishing of silica. All dopants increased the content of Ce^{3+} in the samples. However, although Yb doping led to the highest Ce^{3+} concentration, Nd-doped ceria displayed the best abrasive property. Luo et al. [15] investigated the catalytic oxidation activity of Pr-doped ceria towards CO, CH_4, and CH_3OH. The authors observed that for up to 10% w/w Pr, the catalytic performance improved compared to the pure sample and concluded that oxygen vacancies favor CO oxidation. Over 20% w/w Pr, the authors observed secondary phase formation. Similar results were achieved by Hernández et al. [16], who compared the catalytic response Eu-doped ceria towards CO. The authors reported the formation of secondary phases for Eu contents higher than 17% w/w. Interestingly, the best catalytic performance was observed for 10% w/w Eu. Eu-doped ceria also presented the best performance compared to La- and Gd-doped samples, which was associated with a higher concentration of oxygen vacancies promoted by Eu cations [17]. In another study, Wang et al. [18] investigated the influence of Sm and Gd doping on catalytic CO oxidation. They found that Sm enhanced the catalytic activity of ceria, whereas Gd worsened the performance. Though Gd increased the concentration of oxygen vacancies, the authors stated it is more stable than Sm due to a half-filled 4 f orbital, decreasing CO oxidation. These studies suggest that the concentration of oxygen vacancies or Ce^{3+} atoms does not define the final properties of rare-earth-doped ceria. Understanding the structural modifications promoted by different dopants is crucial to develop better ceria-based materials.

In previous studies, our group has extensively investigated the synthesis and characterization of ceria nanoparticles obtained using the MAH method. Deus et al. [19] studied the influence of NH_4OH, KOH, and NaOH as mineralizing agents on the growth of ceria crystals. KOH and NaOH were the most effective mineralizers, leading to homogeneously distributed nanoparticles with lower aggregation. Deus et al. [20] also studied the effect of soaking time on the synthesis of ceria nanoparticles. They showed that particles with longer soaking time (8 min) exhibited higher crystallization and lower agglomeration than shorter soaking time (1, 2, and 4 min) samples. In another study, Deus et al. [8] reported that the electrical conduction of undoped CeO_2 films thermally treated under vacuum is dominated by the tunneling current, suggesting that the sensor response of CeO_2 in different atmospheres originates from intrinsic defects. In other studies, we investigated how different rare-earth elements and dopant concentration influence the microstructural, optical, and sensing properties of CeO_2. The photoluminescent (PL) emissions of La-doped ceria at higher La concentrations were ascribed to oxygen vacancies created after doping the structure, which shifted the emissions to the low energy range, leading to intense PL emission due to the faster recombination of electrons in Ce 4f and La 3d conduction bands with holes in O 2p valence band [21]. As reported by Oliveira et al. [22], the dopant content in Pr-doped ceria nanoparticles changes the oxygen vacancy and Pr clusters concentration, leading to different color emissions (from blue to white). Rocha et al. [23,24] and Ortega et al. [25] investigated the sensing properties of rare-earth-doped ceria films exposed to different atmospheres, such as dry-air, vacuum, and carbon monoxide. The authors reported a dual CO sensing response (electrical and optical) for La- and Eu-doped ceria, and the shortest response and recovery time to CO were found for 8% w/w dopant concentration. The photoluminescent and magnetic properties of Pr-doped ceria were studied by Cabral et al. [26] and Oliveira et al. [27]. They reported that electronic decays from Pr 5d to O 2p states, oxygen vacancies located near the conduction band, and electron-hole recombination are

responsible for Pr-doped CeO_2 photoluminescent emissions. Oliveira et al. [27] associated the presence of Ce^{3+} cations with the introduction of Pr^{3+} ions into the ceria lattice regardless of Pr concentration, producing a paramagnetic event in the samples.

Pure and doped CeO_2 films have been investigated as a sensing material for different gases, such as NH_3 [28], formaldehyde [29], methanol [30], and oxygen [31]. Carbon monoxide (CO) is particularly problematic: it is odorless, tasteless, colorless, and extremely toxic. Thus, an efficient sensor is essential to prevent potential victims. The use of nanoparticles to prepare sensor films offers a higher CO-surface interaction, improving sensitivity, working temperature, and power consumption [32]. Several methods have been used to synthesize ceria nanostructures, such as sol-gel [33], co-precipitation [34], spray-pyrolysis [35], solvothermal [36], and microwave-assisted hydrothermal [37]. Among these, the microwave-assisted hydrothermal (MAH) technique stands out as an eco-friendly route for obtaining high-quality nanostructures with controlled stoichiometry, particle size, and morphology. Furthermore, when considering large-scale manufacturing of nanoparticles, MAH is a fast, simple, and cost-effective synthesis. Despite the challenges involved in transferring lab-scale production to industrial-scale [38], state-of-the-art microwave digestion systems allow the synthesis of up to 40 samples in the same run, considerably improving scalability. Thus, MAH represents a promising alternative to conventional hydrothermal methods (one of the most used techniques to synthesize oxide nanoparticles [39]), reducing synthesis time and temperature.

In this study, we report the synthesis and characterization of RE-doped (RE = La, Eu) ceria nanoparticles obtained via MAH. The as-prepared nanoparticles were used to prepare thick films using the screen-printing technique. We investigated in detail the modifications imposed by La/ Eu doping in the CeO_2 structure using x-ray diffractometry (XRD), Raman spectroscopy, high-resolution transmission electron microscopy (HRTEM), ultraviolet-visible (UV-Vis) spectroscopy, and photoluminescence (PL) spectroscopy. The films were characterized using field emission-scanning electron microscopy (FE-SEM), and electrical measurements were conducted to evaluate the effect of La/ Eu doping on CeO_2 carbon monoxide sensing response. Our study sheds light on how the different dopants affect the structural, optical, and gas sensing properties of CeO_2 by applying a correlation approach between oxygen vacancy concentration, lattice distortions, exposed facets, and electronic transitions, which have not been discussed in previous works.

2. Experimental procedures

2.1. Synthesis and characterization of the nanoparticles

We used the microwave-assisted hydrothermal method to synthesize $Ce_{1-(3/4)x}RE_xO_2$ (RE = Eu, La; x = 0.0 and 0.08) nanoparticles. First, cerium nitrate hexahydrate ($Ce(NO_3)_3.6H_2O$, Sigma-Aldrich 99.0% pure) was dissolved in deionized water and kept under constant stirring at 70 °C. Simultaneously, the dopant precursors (La_2O_3 or Eu_2O_3, Sigma-Aldrich 99.0% pure) were also dissolved in deionized water (constant stirring, 70 °C) with the addition of nitric acid (HNO_3, Synth 65% pure) to assist dissolution. Then, cerium and Eu/La solutions were mixed and stirred. Then, a 2 M potassium hydroxide (KOH, Synth 99.5% pure) was slowly added to the mixture until pH reached 10. The resulting solution was transferred to a Teflon autoclave, sealed, and placed in a hydrothermal microwave oven (2.45 GHz, 800 W). The synthesis was carried out 100 °C (10 °C/min) for 8 min [26]. Finally, after the system cooled to room temperature, the nanoparticles were washed several times with distilled water and dried at 100 °C for 48 h. Each batch resulted in ~1.7 g of the ceria powder, which corresponds to an 85% yield.

The samples were characterized by x-ray diffraction using a Rigaku-DMax/2500PC diffractometer with Cu-Kα (λ = 1.5406 Å) in
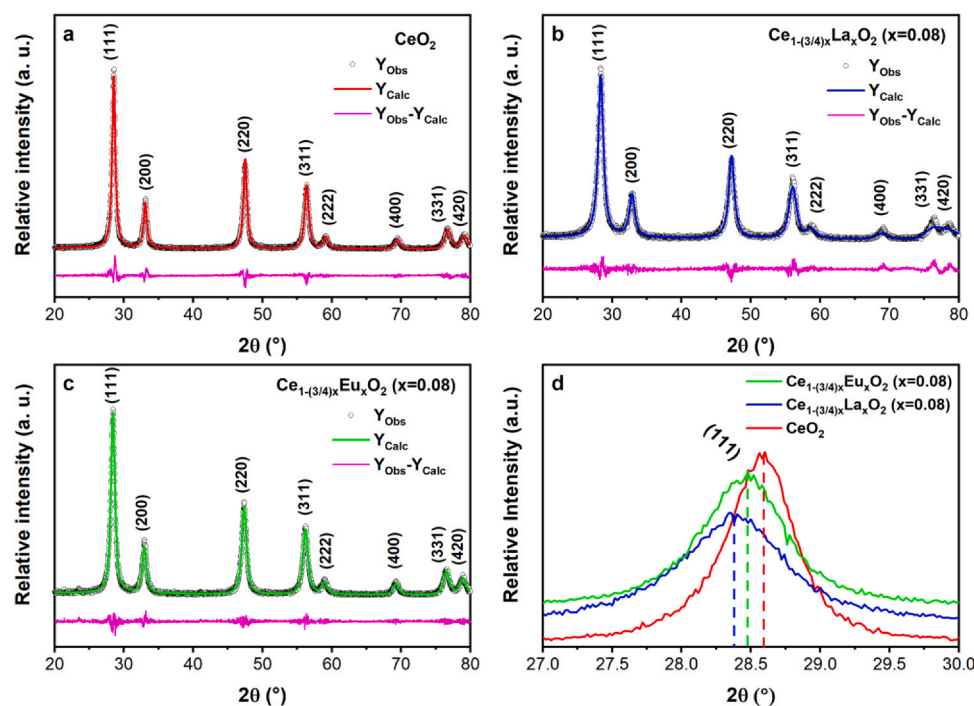
Fig. 1. X-ray diffraction pattern of the pure (a), La-doped (b), and Eu-doped (c) ceria nanoparticles synthesized using the microwave-assisted hydrothermal method at 100 °C for 8 min and shift of the (111) reflection after doping the structure (d).

the 20–80° range and 0.02/min steps. The crystalline structure of the nanoparticles was investigated using TOPAS V5 software [40] and the Rietveld method [41]. We calculated the crystallite size (d) of the samples using Scherrer's equation $d = \lambda.\beta/0.94.cos\theta$, where λ is the wavelength of X-rays, β is the full width at half maximum (FWHM) for (1 1 1) reflection, and θ is the diffraction angle of the main peak. A Lorentzian function was used to fit the peaks, minimizing errors associated with the width (e.g., FWHM) and peak position. The same procedure was used to fit the Raman modes. Raman spectroscopy was carried out in a LabRAM iHR550 Horiba Jobin Yvon spectrometer. The excitation source was an Argon-ion laser ($\lambda = 514$ nm, 8 mW) with a spectral resolution of $1\ cm^{-1}$ and 40 scans in the $100–1000\ cm^{-1}$ range. We used high-resolution transmission electron microscopy (HRTEM) to analyze the size and shape of the nanoparticles. To prepare the samples, the nanoparticles were dispersed in ethanol, dried, and then added to a 300-mesh copper grade, followed by ultrasonic vibration for 5 min. The micrographs were obtained at room temperature in an FEI TECNAI F20 microscope. The specific surface area of the samples was calculated using a Micromeritics ASAP 2010 equipment and the Brunauer-Emmett-Teller (BET) method. The ultraviolet-visible (UV-Vis) spectra were measured in a Cary 5 G (Varian, USA) spectrophotometer in the diffuse reflectance mode. To estimate the bandgap energy of the samples, we used the Kubelka-Munk function to convert the UV-Vis diffuse reflectance data into Tauc plots [42]. The relationship between the bandgap energy and the diffuse reflectance spectrum is given by Eq. (2):

$$[F(R_\infty)h\nu]^{1/n} = B\left(h\nu - E_g\right)$$

(2)

where $F(R_\infty)$ is the Kubelka-Munk function, $h\nu$ is the photon energy, B is a constant, and E_g is the bandgap energy. Parameter n depends on the type of electronic transition of the compound. Considering the electronic transitions in CeO_2 are of the indirect allowed type ($n = 2$), Eq. (2) becomes:

$$[F(R_\infty)h\nu]^{1/2} = B\left(h\nu - E_g\right)$$

(3)

By plotting $[F(R_\infty)h\nu]^{1/2}$ in the y-axis and $h\nu$ in the x-axis, the bandgap energy corresponds to the point where the extrapolation of the linear portion of the curve intercepts the x-axis. Photoluminescence (PL) properties were measured with a Thermal Jarrel-Ash Monospec 27 monochromator and a Hamamatsu R446 photomultiplier. The excitation source was 350.7 nm wavelength of a krypton ion laser (Coherent Innova), keeping their power at 200 mW. All measurements were performed at room temperature. The PL spectra of the pure and doped nanoparticles were converted into a point in the chromaticity diagram (CIE 1931) using Origin® 2019 software.

2.2. Preparation and characterization of the films

To perform the CO sensing tests, we used the RE-doped (RE = La, Eu) ceria nanoparticles obtained using the MAH method to prepare thick films. For each sample, the nanoparticles were mixed with an organic binder (glycerol) in a nanoparticle/binder ratio of 0.6 g/ml to obtain a paste, which was, then, deposited onto insulating alumina (Al_2O_3) substrates using the screen-printing technique. The films were heat-treated at 380 °C for 2 h in a dry air atmosphere with a heating rate of 1 °C/min to evaporate the binder. We used 96% dense alumina substrates with 10×20 mm (width x length) covered by a 25 nm Ti adhesion layer and, on top, a 200 nm Pt layer using RF-Sputtering. The interdigitated Pt electrodes have a $10\ \Omega$ resistance.

FE-SEM microscopy (Supra 35-VP, Carl Zeiss) was carried out to analyze surface morphology and cross-section of the thick films. Electrical characterization and sensing response of the films towards carbon monoxide were conducted in an optoelectronic device developed and patented by our group (Patent INPI Argentina 201501039539/INPI Brazil 10 2016 028383 3 [43,44]). Three heating cycles up to 380 °C in a vacuum were conducted to eliminate

humidity in the samples before the measurements. The film resistance as a function of time was measured to investigate its sensing response towards CO. All measurements were carried out using the two-wire technique, and we used an Agilent 3440 A multimeter to measure sample resistance. Response time (t_{resp}) towards CO represents the time at which there is a 90% resistance drop is from its initial value after the CO flux starts. Similarly, the recovery time (t_{rec}) corresponds to the time in which the film resistance recovered 90% of its initial value after the CO flux is interrupted.

3. Results and discussion

3.1. Characterization of the nanoparticles

3.1.1. X-ray diffractometry (XRD) analysis

Fig. 1 shows the x-ray diffraction (XRD) patterns of the pure and doped ceria samples obtained using the MAH method at 100 °C for 8 min. All reflections were indexed to the cubic fluorite structure of CeO_2 (space group $Fm\bar{3}m$), according to the ICSD file 29046. The absence of reflections belonging to second phases suggests that La^{3+} and Eu^{3+} cations isomorphically substituted Ce^{4+} cations in the lattice. The dopant cations cause an enlargement of the octahedral sites due to their larger ionic radii (Eu^{3+} = 1.066 Å and La^{3+} = 1.16 Å) compared with Ce^{4+} (0.97 Å) [45], resulting in (111) reflection center slightly shifting towards lower 2θ angles, as observed in Fig. 1d [46]. We estimated the crystallite size of the samples using Scherrer's equation (Table 1). Crystallite size decrease after doping may be associated with distortions caused by La^{3+} and Eu^{3+} cations, which would prevent the growth of the crystallites. These distortions are also likely responsible for the slight broadening and intensity decreasing of the peaks compared to the pure sample, indicating that the long-range order of the structure decreased. The Rietveld refinement also shows an increase in the lattice parameter and cell volume proportional to the ionic radius of the dopants [47]. In detail, we noticed that doping with La^{3+} had the largest influence on the ceria structure, decreasing the crystallite size and peak intensity, increasing lattice parameter and cell volume, and broadening and shifting the reflections when compared with the pure and Eu-doped samples. The Rietveld parameters shown in Table 1 confirm the refinement is coherent.
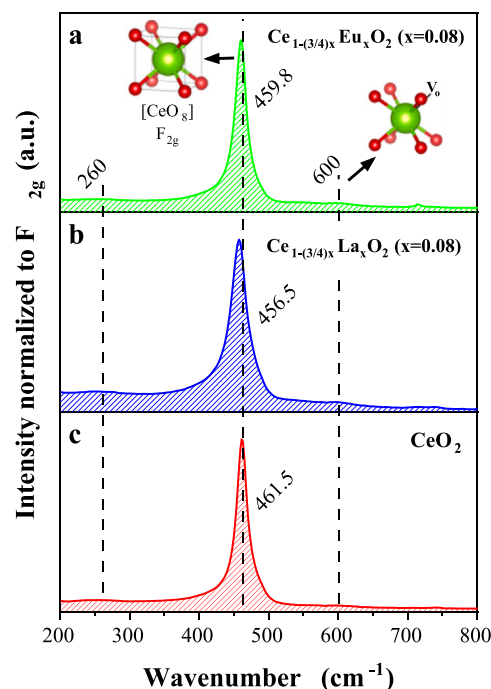
3.1.2. Raman spectroscopy analysis

We investigated phase formation, structural defects, and short-range order-disorder of the nanoparticles using Raman spectroscopy. Ceria crystallizes in a fluorite cubic structure belonging to space group $Fm\bar{3}m$, which has only one active Raman mode near 465 cm^{-1}, corresponding to the triply degenerate F_{2g} symmetric stretching of Ce-O bonds in $[CeO_8]$ units [48]. As illustrated in Fig. 2, this characteristic mode appears in all samples, confirming the formation of the fluorite phase. In pure ceria, the presence of oxygen defects and Ce^{3+} cations changes Ce-O bond lengths, shifting the F_{2g} mode center (461.5 cm^{-1}) towards lower wavenumbers compared to single-crystals (465 cm^{-1}). This behavior concurs with the literature, as observed for ceria samples doped with Eu, Pr, Gd, Sm, and Nd [15,16,46,49]. Likewise, doping the structure changes the lattice parameter due to the different ionic radii of the cations (Ce = 0,97 Å,Eu = 1.066 Å, and La = 1.16 Å) [45], which causes the observed shift

Fig. 2. Raman spectroscopy of the Eu-doped (a), La-doped (b), pure (c) ceria nanoparticles synthesized using the microwave-assisted hydrothermal method at 100 °C for 8 min.
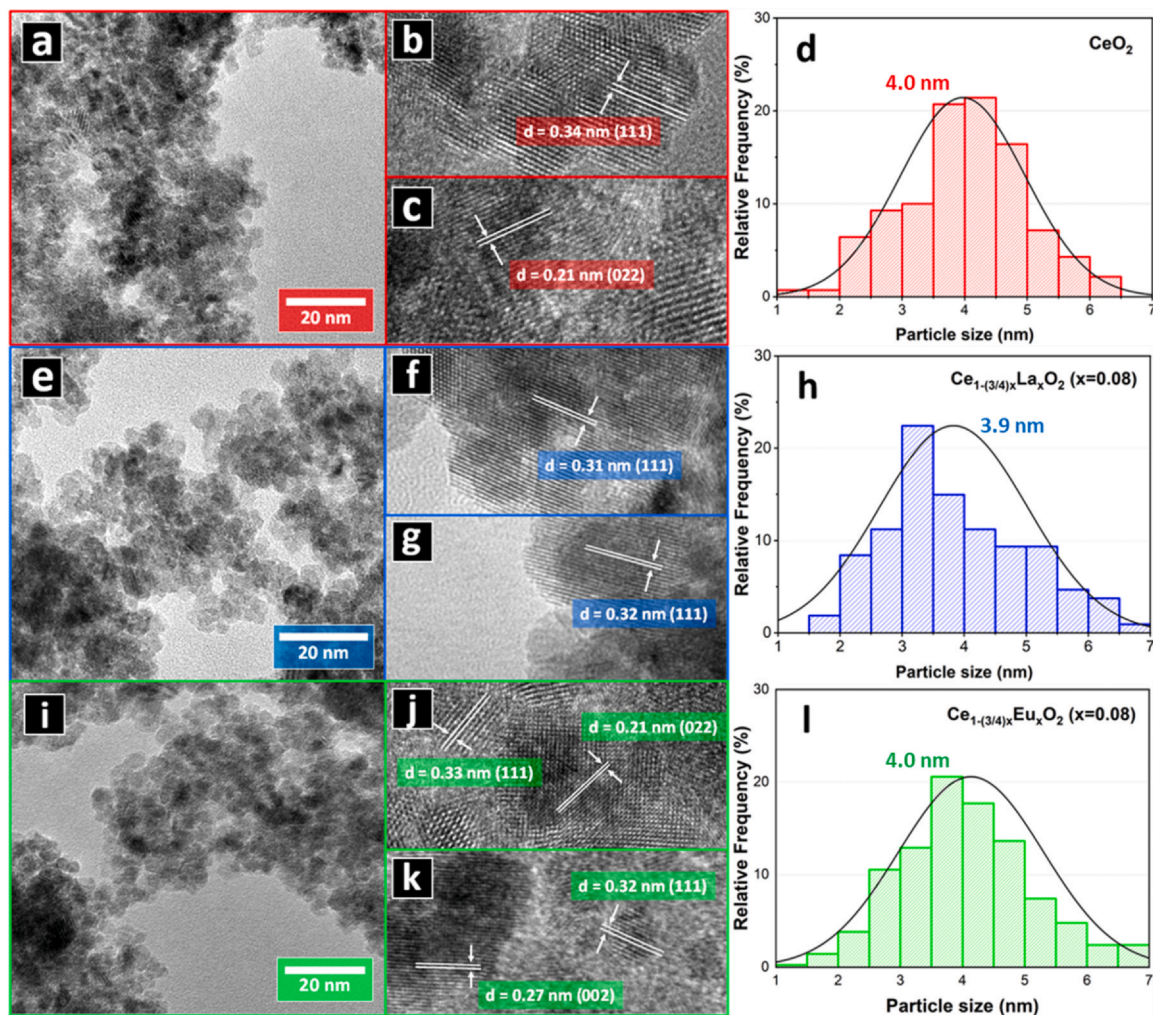
Table 2
P.P. Ortega[a], B. Hangai[a], H. Moreno[a], L.S.R. Rocha[a], M.A. Ramírez[a], M.A. Ponce[b], E. Longo[c], A.Z. Simões[a].

Sample	S_{BET} (m^2/g)
CeO_2	121.3
$Ce_{1-(3/4)x}La_xO_2$ (x = 0.08)	89.4
$Ce_{1-(3/4)x}Eu_xO_2$ (x = 0.08)	88.7

in the center of the F_{2g} mode to 456.5 and 459.8 cm^{-1} in La- and Eu-doped samples, respectively (Table 2). Table 2 also depicts the calculated FWHM values for F_{2g} mode, indicating that the shape becomes broader for La- and Eu-doped nanoparticles, especially the La-doped sample, which may be associated with the expansion of the octahedral sites, decreasing short-range symmetry in the doped structures [50]. Mode shape is also affected by the presence of oxygen vacancies, suggesting the structure is non-stoichiometric. The nanometric scale of the particle also influences the curve shape of the Raman mode [51].

The $[CeO_8]$ arrangement is sensitive to disorders in the oxygen sublattice, which should be independent of the cation mass since only oxygen atoms move in the ceria structure [52]. Therefore, we attribute the weak mode around 600 cm^{-1} to oxygen vacancies (also known as the defect-induced mode or D-mode). These vacancies probably originate from two processes: intrinsic Ce^{4+} to Ce^{3+} reduction; and the incorporation of La^{3+} or Eu^{3+} cations at Ce^{4+} sites in the CeO_2 structure. Both produce oxygen vacancies to compensate for the charge difference between the trivalent cations (Ce^{3+}, La^{3+}, and Eu^{3+}) and Ce^{4+}. We can estimate the concentration of oxygen

Table 1
P.P. Ortega[a], B. Hangai[a], H. Moreno[a], L.S.R. Rocha[a], M.A. Ramírez[a], M.A. Ponce[b], E. Longo[c], A.Z. Simões[a].

Sample	Geometry parameters		Rietveld parameters			Crystallite size (nm)
	V (Å^3)	phase (%)	R_{bragg}	R_{wp}	χ^2	
CeO_2	158.59	100.0	1.35	13.75	1.26	15.4
$Ce_{1-(3/4)x}La_xO_2$ (x = 0.08)	159.20	100.0	1.89	13.04	1.13	9.6
$Ce_{1-(3/4)x}Eu_xO_2$ (x = 0.08)	160.64	100.0	2.26	13.88	1.28	12.4

Fig. 3. High-resolution transmission electron microscopy, d-spacings, and particle size distribution of the pure (a-d), La-doped (e-h), and Eu-doped (i-l) ceria nanoparticles synthesized using the microwave-assisted hydrothermal method at 100 °C for 8 min.

vacancies by calculating the intensity ratio of the modes near 465 and 600 cm^{-1} (I$_D$/I$_{F_{2g}}$); higher ratios are associated with higher content of oxygen vacancies in the lattice [53]. As expected, we found that doping the structure led to higher concentrations of oxygen vacancies, reflected by the higher I$_D$/I$_{F_{2g}}$ ratios for La- and Eu-doped samples when compared with the pure sample (Table 2). The absence of Raman modes associated with Eu$_2$O$_3$ (Fig. 2a) and La$_2$O$_3$ (Fig. 2b) reinforces the formation of a complete solid solution, as observed in the XRD analysis. Finally, a doubly degenerate transverse optical mode and disorders in the structure are responsible for the weak vibrational mode observed at 260 cm^{-1} [54].

3.1.3. Morphological analysis of the nanoparticles

Fig. 3 illustrates the high-resolution transmission electron microscopy (HRTEM) of the pure and doped nanoparticles synthesized using the MAH method. From Fig. 3a, e, and 3i, we observed the samples show a sphere-like morphology, which seems to be independent of the dopant cations. The final morphology of the nanoparticles is defined by nucleation-dissolution-recrystallization processes, which are controlled by parameters such as time, temperature, and base (OH) concentration [55]. At the beginning of the MAH synthesis, multiple nucleation sites are formed in the solution, in which Ce(OH)$_4$ hydroxides are deprotonated and converted into CeO$_2$ [19]. In low-base concentrations, low temperature, and short synthesis time, the dissolution-recrystallization rate is slow, leading

to the formation of irregular spherical-shaped nanostructures, which is the case. By increasing synthesis temperature, time, or base concentration, the dissolution-recrystallization rate increases, and different nanostructures can be obtained, as reported in the literature [7,37,56].

The atomic resolution images containing the interplanar distances (d-spacing) of the undoped, La-doped, and Eu-doped nanoparticles are shown in Fig. 3b-c, Fig. 3f-g, and Fig. 3j-k, respectively. The d-spacings corresponding to the (1 1 1) planes consist of a planar distribution of Ce and O atoms, and it is the most stable surface of ceria [57]. The (0 2 2) and (0 0 2) planes are corrugated, and either Ce or O atoms are exposed on the surface. These three planes are the most common facets of ceria [58]. For the pure sample (Fig. 3b-c), the d-spacings correspond to (1 1 1) planes and, to a smaller extent, (0 2 2) planes. The La-doped sample (Fig. 3f-g) shows only (1 1 1) facets, and (1 1 1) facets dominate the surface of the Eu-doped nanoparticles, while there are traces of (2 2 0) and (0 0 2) facets. The different facets of the samples may be related to distortions introduced in the lattice due to defects and the higher ionic radius of the dopants.

The particle size distributions of the pure and doped ceria are shown in Fig. 3d, h, and l. For all samples, the size of the nanoparticles homogeneously varies over a few nanometers, with an average particle size of ~ 4 nm. As the synthesis takes place in a highly diluted solution during the MAH method, after nucleation, there are not enough reactants left in solution to promote crystal

Table 3

P.P. Ortega[a], B. Hangai[a], H. Moreno[a], L.S.R. Rocha[a], M.A. Ramírez[a], M.A. Ponce[b], E. Longo[c], A.Z. Simões[a].

| Sample	F_{2g} wavelength (cm⁻¹)	$I_D/I_{F_{2g}}$	F_{2g} FWHM
CeO_2	461.52	0.036	21.73
$Ce_{1-(3/4)x}La_xO_2$ (x = 0.08)	456.48	0.057	33.49
$Ce_{1-(3/4)x}Eu_xO_2$ (x = 0.08)	459.82	0.054	22.07

growth, resulting in nanoparticles with a reduced size distribution [25]. Nanoparticles usually exhibit high surface free energy due to their nanometric scale, which leads to a strong tendency to form large agglomerates, minimizing surface energy. At the nanoscale, van der Waals forces are significant and contribute to the agglomeration state of the nanoparticles.

The specific surface area is an essential parameter for materials whose properties rely on reactions occurring on the surface. For gas sensing applications, larger specific surface areas mean more sites are available for molecular adsorption of the target gas, which improves their sensibility and response. We used the Brunauer-Emmett-Teller (BET) method to calculate the specific surface areas (S_{BET}) of the samples (Table 3). The doped samples exhibited a lower surface area compared with the pure sample. It might be associated with a higher agglomeration of the doped nanoparticles due to higher surface energies and size distribution. Hwang et al. [59] synthesized CeO_2 nanoparticles using a combustion route and obtained S_{BET} values between 40 and 65 m²/g. In another study, Fu et al. [60] obtained similar S_{BET} using microwave-induced combustion (43 m²/g) and precipitation (48 m²/g) methods to prepare CeO_2 nanoparticles. Lu et al. [61] used the sol-gel method to obtain pure and Co-doped ceria, which resulted in S_{BET} values of 39 and 75.1 m²/g, respectively. Higher S_{BET} were found by Srivastava et al. [62] using a hydrothermal route. The authors obtained ceria nanoparticles with S_{BET} values of 120 m²/g for samples calcined at 450 °C and 78 m²/g when calcined at 650 °C. Considering the specific surface area discussed above, the MAH method used in this study led to nanoparticles with relatively high S_{BET}, with the advantage of being a fast and low-temperature synthesis technique.

3.1.4. Ultraviolet-visible (UV-Vis) spectroscopy analysis

The Tauc plots and estimated bandgap energies (E_{gap}) of the pure and doped nanoparticles are shown in Fig. 4. The bandgap represents the forbidden energy region between the highest energetic level of the valence band and the lowest energetic level of the conduction band. In ceria-based materials, it corresponds to the energy difference between O 2p and Ce 5d states. However, cerium cations in CeO_2 can easily reduce from Ce^{4+} to Ce^{3+}, creating oxygen vacancies to compensate for the charge variation. During this process, electrons previously localized in the O 2p states move to empty Ce 4f states, creating intermediary levels within the bandgap. These intermediate transitions reduce the energy required to excite electrons from the valence band, thus decreasing the bandgap energy value. In the samples synthesized in this study, the electrons are localized in the 4f states situated inside the bandgap and above the Fermi energy level instead of the conduction band. In what follows, we refer to the effective energy gap as the energy needed for the excitation of an electron from the uppermost energetic level of the valence band to the 4f states.

Fig. 4 shows the estimated bandgap energies (E_{gap}) of the nanoparticles. The E_{gap} corresponds to the point where the extrapolation of the linear portion of the Tauc plot intercepts the x-axis. The E_{gap} for the pure ceria nanoparticles (Fig. 4c) is consistent with the values reported in the literature [51,63]. After doping the structure, the E_{gap} slightly decreases (Fig. 4a and b), following the order: pure (3.10 eV) > La-doped (3.00 eV) > Eu-doped (2.93 eV). This reduction is expected since the substitution of Ce^{4+} cations by La^{3+} and Eu^{3+}
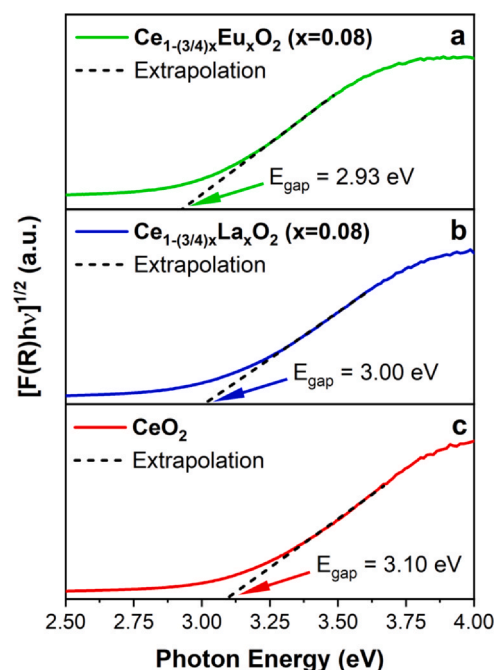

Fig. 4. Bandgap energies calculated from the UV-Vis diffuse reflectance spectra of the Eu-doped (a), La-doped (b), pure (c) ceria nanoparticles synthesized using the microwave-assisted hydrothermal method at 100 °C for 8 min.

cations narrows the gap energy between O 2p and Ce 4f states [25]. This narrowing effect results from an increase in the density of states between the conduction and the valence band due to the formation of Ce 4f¹ and oxygen vacancies [11]. The studies of Amoresi et al. [7] and Oliveira et al. [37] have shown that the morphology of CeO_2 nanostructures can also influence the bandgap. They obtained different undoped CeO_2 nanostructures and suggested the E_{gap} depends on the exposed surface morphology. Particle size distribution [51] can also influence the E_{gap} values. As shown in Fig. 3, the Eu-doped sample exhibits different facets compared with the pure and La-doped systems, which can be associated with its smaller bandgap value.

3.1.5. Photoluminescence (PL) spectroscopy analysis

The normalized PL spectra of the nanoparticles are exhibited in Fig. 5a. In ceria-based compounds, when an oxygen vacancy forms (due to intrinsic or extrinsic mechanisms), a pair of electrons gets trapped in the vacancy site, creating F centers. These oxygen defect states appear below Ce 4f states, which are assigned to the emission spectrum [64]. For the pure CeO_2 nanoparticles, there is a broad band centered at 460 nm (blue-green region) with a second, weaker band close to 600 nm (orange region). The blue-green emissions can be associated with the direct recombination of holes in O 2p states with electrons in Ce 4f states [21,26] and surface defects in the nanostructures [65]. The broadness of the band may be ascribed to a high quantity of defects, linked to oxygen vacancies and Ce^{3+} cations in the structure, indicating some structural order-disorder level [21,64]. The weak band assigned to orange emissions can be related to the distribution of defects near the conduction band, defined as shallow defects [27]. The La-doped sample shows a similar spectrum, with bands associated with blue-green and orange regions, indicating that the same mechanisms are responsible for these emissions in both La-doped and undoped samples. However, the La-doped bands are sharper and more pronounced, indicating a stronger influence of oxygen vacancies, Ce 4f intermediate levels, and shallow defects, which agrees with the Raman and UV-Vis data.

(a)

(b)
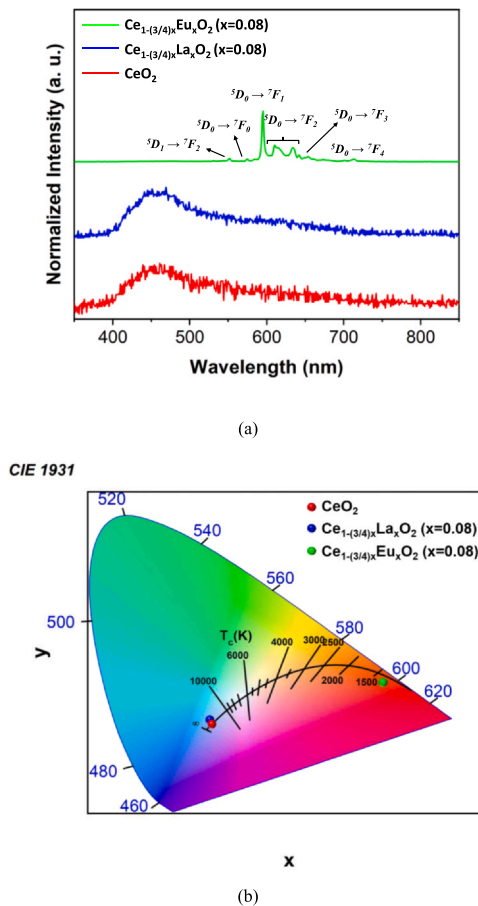
Fig. 5. Photoluminescence spectroscopy (a) and CIE chromaticity diagram (b) of the pure, La-doped, and Eu-doped ceria nanoparticles synthesized using the microwave-assisted hydrothermal method at 100 °C for 8 min.

The PL spectrum (Fig. 5a) of the Eu-doped nanoparticles is significantly different from the previous samples, showing sharp bands between 550 and 750 nm. These bands are associated with inter-configurational f-f electronic transitions ($^5D_0 \rightarrow {}^7F_J$) of the Eu^{3+} ions as follows: 570 ($J = 0$), 593 ($J = 1$), 610 and 630 ($J = 2$), 650 ($J = 3$), and 710 nm ($J = 4$) [66]. The Eu^{3+} ions are hypersensitive to the crystal field, in a way that the PL emissions provide information about the host matrices structure and local symmetry [67]. The $^5D_0 \rightarrow {}^7F_1$ transitions correspond to magnetic dipole transitions and are insensitive to the local crystal field around Eu^{3+}. Contrarily, $^5D_0 \rightarrow {}^7F_2$ transitions correspond to electronic dipole transitions, which are hypersensitive to the crystal field around the sites occupied by Eu^{3+} [68]. In CeO$_2$, Ce^{4+} sites display O$_h$ symmetry and are coordinated by eight oxygen ions. Therefore, the Ce^{4+} sites have an inversion symmetry [69]. It is known from the literature [70] that inversion symmetry does not allow electric dipole transitions ($^5D_0 \rightarrow {}^7F_2$) in Eu^{3+}, but it does not affect magnetic dipole transitions; therefore, magnetic dipole transitions ($^5D_0 \rightarrow {}^7F_1$) dominate the emissions of our samples with a high-intensity band at 593 nm. However, the doping process creates oxygen vacancies to compensate for the charge difference between Eu^{3+} and Ce^{4+}, inducing symmetry distortions that partially allow electric dipole transitions, resulting in the low-intensity emissions (D$_0 \rightarrow {}^7F_2$ and $^5D_0 \rightarrow {}^7F_3$) observed in the PL spectrum [70]. These symmetry distortions increase CeO$_2$ conductivity [69], stimulating a sensing response. In addition, from the intensity ratio between ($^5D_0 \rightarrow {}^7F_1$)/($^5D_0 \rightarrow {}^7F_2$) and the ($^5D_1 \rightarrow {}^7F_2$) and ($^5D_0 \rightarrow {}^7F_0$) bands at 550 and 575 nm, respectively, we can assume that Eu^{3+} replaces Ce^{4+} in the octahedral sites, being the only sites occupied by Eu^{3+} cations in the lattice [68,69,71].

Based on the PL spectra of the samples, we estimated the emission color using the *Commission Internationale de l'Eclairage* (CIE) chromaticity diagram (Fig. 5b). Pure and La-doped ceria (red and blue spheres, respectively) emitted light in the blue region, close to the white light region. The Eu-doped nanoparticles (green sphere) emitted light in the orange-red region. Malleshappa et al. [64] have synthesized Eu-doped ceria nanostructures by controlling the dopant concentration and found excellent red light emission properties. Oliveira et al. [22] synthesized Pr-doped ceria nanoparticles using the MAH method and reported different color emissions depending on the Pr concentration, shifting from blue to white light. Therefore, by doping the ceria structure with different rare-earth elements, such as La and Eu, it is possible to control its optical properties, which is interesting to produce white light LED as blue and red components.

3.2. Characterization of the thick films

3.2.1. Field-emission scanning electron microscopy (FE-SEM) analysis

The top view and cross-section micrographs of the pure and doped thick films obtained using FE-SEM are shown in Fig. 6. We observed the nanoparticles tend to form large agglomerates compared to the average particle size shown in Fig. 3. This behavior is expected due to the use of an organic binder (glycerol) for mixing the nanoparticles before depositing the thick films. The OH groups present in the binder increase the van der Waals forces between the nanoparticles, resulting in a high agglomeration state (Fig. 6, top view). Han et al. [72] prepared Yb- and Er-doped ceria films by the
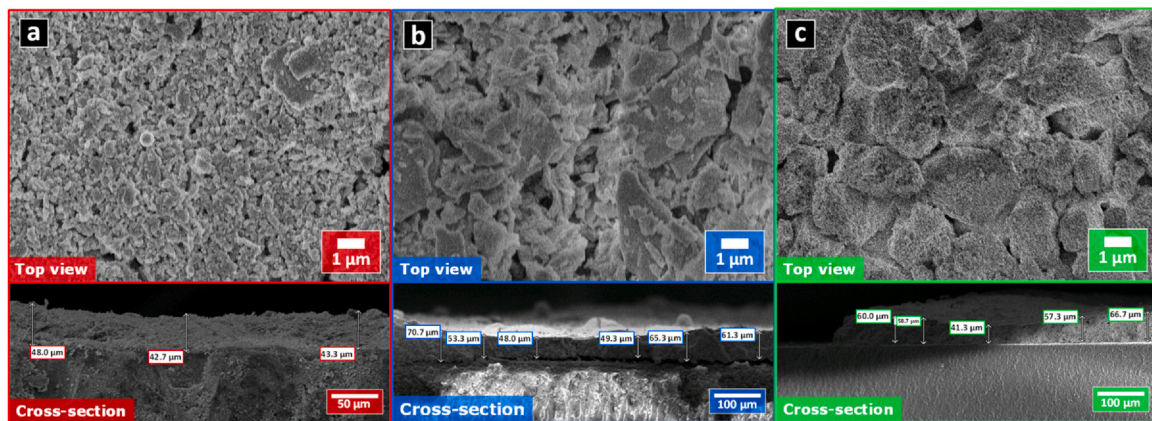
Fig. 6. Field-emission scanning electron microscopy of the top view and cross-section of the thick films prepared from pure (a), La-doped (b), and Eu-doped (c) ceria nanoparticles synthesized using the microwave-assisted hydrothermal method at 100 °C for 8 min.
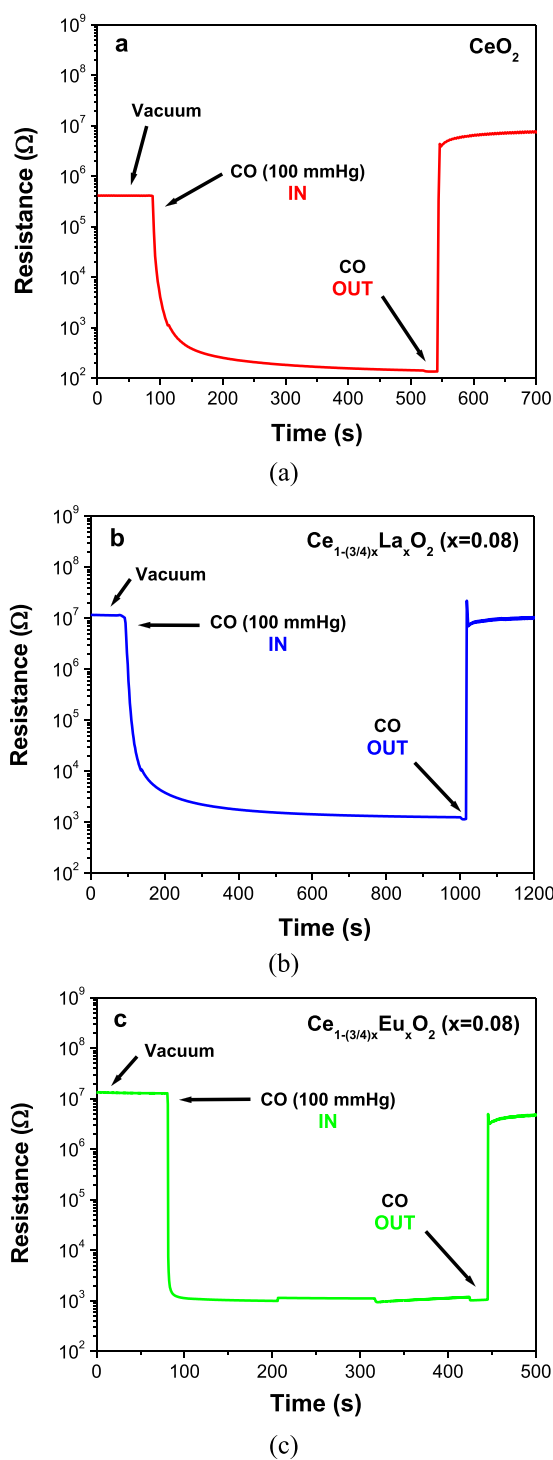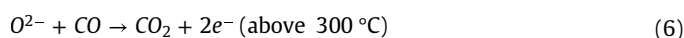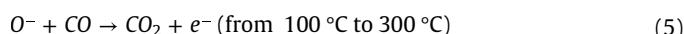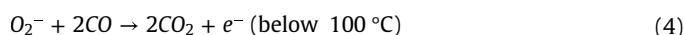
Fig. 7. Resistance in function of time and atmosphere of the thick films prepared from pure (a), La-doped (b), and Eu-doped (c) ceria nanoparticles synthesized using the microwave-assisted hydrothermal method at 100 °C for 8 min.

screen-printing technique using ethanol and terpineol as binders. The authors observed the formation of micrometric agglomerates with rounded morphology, confirming the influence of binders in the agglomeration state of the films during their preparation. Micrographs of the thick films cross-section (Fig. 6 - cross-section) show an average thickness varying from ~40 to ~60 µm. For gas sensing applications, the long distance between the reaction sites on the surface of the films to the Pt electrodes at the bottom can reduce the dynamic response of the sensor [73]. This effect is lessened in

our samples due to porosity, as observed in Fig. 6 - top view, which also improves adsorption and, hence, the sensing response towards the target gas.

3.2.2. Electrical characterization of the films

The films electrical response during interaction with vacuum, dry air, and CO atmospheres is presented in Fig. 7. Carbon monoxide detection by the sensing films involves different reactions depending on the temperature. For n-type semiconductors such as ceria-based materials, three oxygen ions (superoxides, peroxides, and monoxides) may form on the surface as the temperature of the system increases: O_2^- (below 100 °C), O^- (from 100° to 300°C), and O^{2-} (above 300 °C). These adsorbed species trap electrons from the conduction band, increasing the film resistance. When exposed to a CO atmosphere, they react with each other to form CO_2, and the trapped electrons move back to the conduction band, decreasing film resistance. Since O_2^-, O^- and O^{2-} have different oxidation states (−1/2, −1, and −2, respectively), the resistance drop is more pronounced at temperatures above 300 °C due to the higher number of electrons involved, as shown in Eqs. (4)–(6) [8]:

$$O_2^- + 2CO \rightarrow 2CO_2 + e^- \text{ (below } 100 °C) \tag{4}$$

$$O^- + CO \rightarrow CO_2 + e^- \text{ (from } 100 °C \text{ to } 300 °C) \tag{5}$$

$$O^{2-} + CO \rightarrow CO_2 + 2e^- \text{ (above } 300 °C) \tag{6}$$

Therefore, resistance changes in the films when exposed to air or CO atmospheres provide a measurable response, which allows the detection of $CO_{(g)}$.

Fig. 7 shows the electrical response of the films measured at 380 °C in terms of the resistance variation as a function of time. By comparing the initial resistance of the films in vacuum (t = 0 s), we observed that the doped samples exhibited higher values compared to pure ceria, indicating the doping process led to higher resistivity. To understand this behavior, we must know that the La^{3+} and Eu^{3+} ions substitute Ce^{4+} in the CeO_2 structure and act as acceptor states, partially compensating the Ce 5d donor states in the bandgap due to the presence of oxygen vacancies (also acts as donor states). Therefore, the resistivity of the films increases.

When carbon monoxide is pumped into the gas chamber, the reaction showed in Eq. (6) provokes a rapid electrical resistance decrease. The calculated response time (t_{resp}, necessary for a 90% decrease in resistance before CO flux is introduced) towards CO was: 6.6 s (pure CeO_2), 4.2 s (La-doped), and 1 s (Eu-doped), as shown in Table 4. Multiple factors might explain the t_{resp} decrease, such as particle size, film thickness, porosity, and morphology. As discussed previously, the interaction between the gaseous molecules and the surface of the films is crucial to understand their behavior [74]. In Fig. 3, we showed that the Eu-doped nanoparticles exhibit different facets compared to pure and La-doped samples. La-doped nanoparticles have mostly (111) facets, the lowest energy surfaces (1.19 J.m^{-2} [7]), making it the most stable ceria surface. On the other hand, besides (111) facets, Eu-doped nanoparticles also present (002) (2.26 J.m^{-2} [7]) and (022) (1.60 J.m^{-2} [7]) facets, which may favor CO-surface interactions, enhancing response time (Fig. 7c).

During the exposure to a reducing atmosphere (as $CO_{(g)}$), net oxygen can move from the bulk to the surface (oxygen out of the grain diffusion) reacting with CO. This process originates an oxygen

Table 4

P.P. Ortega[a], B. Hangai[a], H. Moreno[a], L.S.R. Rocha[a], M.A. Ramírez[a], M.A. Ponce[b], E. Longo[c], A.Z. Simões[a].

Sample	T_{resp} (s)	T_{rec} (s)
CeO_2	6.6	56
$Ce_{1-(3/4)x}La_xO_2$ (x = 0.08)	4.2	39
$Ce_{1-(3/4)x}Eu_xO_2$ (x = 0.08)	1.0	15

vacancy at the lattice. These vacancies act as donors, thus, increasing the number of charge carriers and reducing the resistance values, as observed in Fig. 7. The opposite behavior is expected after the CO flux is interrupted. Deus et al. [8] proposed that at temperatures above 200 °C, oxygen species adsorbed on the surface can move into the bulk, annihilating oxygen vacancies and reducing the number of charge carriers available. This process rapidly increases films resistivity, as observed in the last region of Fig. 7. The calculated recovery time (t_{rec}, time necessary for resistance to increase to 90% its value after CO flux is interrupted) of the samples was: 56 s (pure CeO_2), 39 s (La-doped), and 15 s (Eu-doped).

Potential barrier located at grain boundaries (known as Schottky barriers) has been considered a key parameter to understand the electrical conductivity mechanisms of n-type semiconductors, such as SnO_2 [75]. However, the electrons responsible for ceria conductivity belong to the inner f states, which tend to form extremely narrow bands. Therefore, these electrons migrate through the structure by a hopping mechanism described by Tuller et al. [76]. The hopping mechanism is a quantum tunneling process in which electrons hop from one localized state to another localized state by absorbing or emitting phonons [77]. This means that charge carriers can be thermally created by exciting electrons through the bandgap as well as localized states can thermally create charge carriers. In high-quality crystals, defect densities are too low to allow hopping conduction. Thus, doping the structure extrinsically increases defect density and localized states, making conduction by hopping and tunneling mechanisms possible [8,78]. Also, since the electrical conductivity of rare-earth oxides belongs to incomplete d or f orbitals, there is a tendency to form small polarons due to slight electron overlapping. Small polarons are defects caused by the displacement of atoms near a trapped charge carrier (electrons, in our case). Then, both the charge carrier and distortion migrate through the lattice by an activated hopping mechanism [76]. Since oxygen vacancies are the predominant defect in our samples, we expect them to be the main contributor to the conductivity by hopping mechanisms [79].

The results compiled in Table 4 show the sensing responses obtained in this study. Durrani et al. [80] prepared CeO_2 thin films at 500 °C and tested their behavior towards CO sensing. Temperatures between 300 and 500 °C and CO concentrations between 500 and 50,000 ppm were used. The authors concluded that the best working temperature was 390 °C (similar to the one used in our study). They also reported a response and recovery time of 45 and 25 s, respectively. Izu et al. [81] studied CeO_2 thick films synthesized in different temperatures (800–1100 °C), and the best result was found at 450 °C and 5000 ppm. In this case, the response time and particle size distribution were 2 s and 58 nm, respectively. In another study [82], they reported a response time of 47 s and a recovery time of 53 s. Mena et al. [83] used the co-precipitation technique to synthesize CeO_2 microspheres and prepare sensing devices. The authors were able to detect 200 ppm of CO at 275 °C in 9 s. Therefore, ceria nanoparticles prepared via MAH are a promising alternative for CO sensing, enhancing electrical response compared to other works in the literature.

4. Conclusions

In this study, we synthesized $Ce_{1-(3/4)x}RE_xO_2$ (RE = La, Eu; x = 0.00 and 0.08) nanoparticles using the microwave-assisted hydrothermal (MAH) method. X-ray diffraction analysis of the nanoparticles confirmed formation of the cubic fluorite phase of ceria, and the doping process did not result in secondary phases. Doping the structure caused unit cell distortions, leading to lattice expansion, which was ascribed to the larger ionic radii of La^{3+} and Eu^{3+} incorporated at the Ce^{4+} sites in the CeO_2 structure. Raman spectroscopy revealed the presence of oxygen vacancies as the dominant defect in the samples. High-resolution transmission microscopy showed the nanoparticles

have a sphere-like morphology and reduced particle size distribution, commonly associated with the MAH method depending on the synthesis parameters. Eu-doped sample presented facets with higher surface energy compared with the pure and La-doped samples. The introduction of Eu^{3+} and La^{3+} in the lattice reduced the bandgap energy of pure ceria in 0.17 eV (Eu-doped) and 0.10 eV (La-doped). Doping with La and Eu modified ceria photoluminescent properties, leading to blue (La) and red (Eu) emissions. The thick films prepared using the as-prepared nanoparticles displayed a measurable response in terms of resistivity during exposition to vacuum, dry air, and carbon monoxide atmospheres. Eu-doped sample responded much faster (1 s) to carbon monoxide compared to La-doped (4.2 s), and pure ceria (6.6 s). This behavior was attributed to the higher surface energy and electronic transitions in the Eu-doped films associated with possible particle size, film thickness, exposed facets, and porosity contributions. We suggest that hopping mechanisms dominate the conduction of the Eu-doped sample. Therefore, doping the ceria structure led to an improvement in its photoluminescent and gas sensing properties, making it a promising material for white LED components and CO gas sensing devices.

CRediT authorship contribution statement

P. P. Ortega: Writing − original draft preparation, Formal analysis. **B. Hangai:** Writing − review & editing. **H. Moreno:** Formal analysis, Writing − review & editing. **L.S.R. Rocha:** Formal analysis, Writing − review & editing. **M. A. Ramirez:** Formal analysis, Writing − review & editing. **M. A. Ponce:** Conceptualization, Formal analysis. **E. Longo:** Resources, Supervision. **A.Z. Simões:** Conceptualization, Methodology, Supervision.

Declaration of Competing Interest

The authors declare that they have no known competing financial interests or personal relationships that could have appeared to influence the work reported in this paper.

Acknowledgments

References

[1] J. Calvache-Muñoz, F.A. Prado, J.E. Rodríguez-Páez, Cerium oxide nanoparticles: synthesis, characterization and tentative mechanism of particle formation, Colloids Surf. A Physicochem. Eng. Asp. 529 (2017) 146–159, https://doi.org/10.1016/j.colsurfa.2017.05.059

[2] B. Choudhury, A. Choudhury, Ce^{3+} and oxygen vacancy mediated tuning of structural and optical properties of CeO_2 nanoparticles, Mater. Chem. Phys. 131 (2012) 666–671, https://doi.org/10.1016/j.matchemphys.2011.10.032

[3] P. Li, X. Chen, Y. Li, J.W. Schwank, A review on oxygen storage capacity of CeO_2-based materials: influence factors, measurement techniques, and applications in reactions related to catalytic automotive emissions control, Catal. Today 327 (2019) 90–115, https://doi.org/10.1016/j.cattod.2018.05.059

[4] L. Li, B. Zhu, J. Zhang, C. Yan, Y. Wu, Electrical properties of nanocube CeO_2 in advanced solid oxide fuel cells, Int. J. Hydrog. Energy 43 (2018) 12909–12916, https://doi.org/10.1016/j.ijhydene.2018.05.120

[5] K. Rajesh, P. Sakthivel, A. Santhanam, J. Venugobal, Incorporation of silver ion on structural and optical characteristics of CeO_2 nanoparticles: white LED applications, Optik 216 (2020) 164800, https://doi.org/10.1016/j.ijleo.2020.164800

[6] A.T. Apostolov, I.N. Apostolova, J.M. Wesselinowa, Co, Fe and Ni ion doped CeO_2 nanoparticles for application in magnetic hyperthermia, Phys. E: Low. -Dimens. Syst. Nanostruct. 124 (2020) 114364, https://doi.org/10.1016/j.physe.2020.114364

[7] R.A.C. Amoresi, R.C. Oliveira, N.L. Marana, P.B. De Almeida, P.S. Prata, M.A. Zaghete, E. Longo, J.R. Sambrano, A.Z. Simões, CeO_2 nanoparticle morphologies and their corresponding crystalline planes for the photocatalytic degradation of organic pollutants, ACS Appl. Nano Mater. 2 (2019) 6513–6526, https://doi.org/10.1021/acsanm.9b01452

[8] R.C. Deus, R.A.C. Amoresi, P.M. Desimone, F. Schipani, L.S.R. Rocha, M.A. Ponce, A.Z. Simoes, E. Longo, Electrical behavior of cerium dioxide films exposed to different gases atmospheres, Ceram. Int. 42 (2016) 15023–15029, https://doi.org/10.1016/j.ceramint.2016.06.151

[9] T. El-Achari, F. Goumrhar, L.B. Drissi, R.A. Laamara, Structural, electronic and magnetic properties of Mn doped CeO_2: an ab-initio study, Phys. B: Condens. Matter 601 (2021) 412443, https://doi.org/10.1016/j.physb.2020.412443

[10] B. Soni, S. Makkar, S. Biswas, Effects of surface structure and defect behavior on the magnetic, electrical, and photocatalytic properties of Gd-doped CeO_2 nanoparticles synthesized by a simple chemical process, Mater. Charact. 174 (2021) 110990, https://doi.org/10.1016/j.matchar.2021.110990

[11] S. Kumar, K. Kumari, F.A. Alharthi, F. Ahmed, R.N. Aljawfi, P.A. Alvi, R. Kumar, M. Hashim, S. Dalela, Investigations of TM (Ni, Co) doping on structural, optical and magnetic properties of CeO_2 nanoparticles, Vacuum 181 (2020) 109717, https://doi.org/10.1016/j.vacuum.2020.109717

[12] M. Michalska, K. Lemański, A. Sikora, Spectroscopic and structural properties of CeO_2 nanocrystals doped with La^{3+}, Nd^{3+} and modified on their surface with Ag nanoparticles, Heliyon 7 (2021) 06958, https://doi.org/10.1016/j.heliyon.2021.e06958

[13] A. Balamurugan, M. Sudha, S. Surendhiran, R. Anandarasu, S. Ravikumar, Y.A. Syed Khadar, Hydrothermal synthesis of samarium (Sm) doped cerium oxide (CeO_2) nanoparticles: Characterization and antibacterial activity, Mater. Today Proc. Elsevier Ltd, 2019, pp. 3588–3594, https://doi.org/10.1016/j.matpr.2019.08.217

[14] J. Cheng, S. Huang, Y. Li, T. Wang, L. Xie, X. Lu, RE (La, Nd and Yb) doped CeO_2 abrasive particles for chemical mechanical polishing of dielectric materials: experimental and computational analysis, Appl. Surf. Sci. 506 (2020) 144668, https://doi.org/10.1016/j.apsusc.2019.144668

[15] M.F. Luo, Z.L. Yan, L.Y. Jin, Structure and redox properties of $Ce_xPr_{1-x}O_{2-\delta}$ mixed oxides and their catalytic activities for CO, CH_3OH and CH_4 combustion, J. Mol. Catal. A Chem. 260 (2006) 157–162, https://doi.org/10.1016/J.MOLCATA.2006.07.012

[16] W.Y. Hernández, M.A. Centeno, F. Romero-Sarria, J.A. Odriozola, Synthesis and characterization of $Ce_{1-x}Eu_xO_{2-x/2}$ mixed oxides and their catalytic activities for CO oxidation, J. Phys. Chem. C. 113 (2009) 5629–5635, https://doi.org/10.1021/JP8092989

[17] W.Y. Hernández, O.H. Laguna, M.A. Centeno, J.A. Odriozola, Structural and catalytic properties of lanthanide (La, Eu, Gd) doped ceria, J. Solid State Chem. 184 (2011) 3014–3020, https://doi.org/10.1016/j.jssc.2011.09.018

[18] Z. Wang, Q. Wang, Y. Liao, G. Shen, X. Gong, N. Han, H. Liu, Y. Chen, Comparative study of CeO_2 and doped CeO_2 with tailored oxygen vacancies for CO oxidation, ChemPhysChem 12 (2011) 2763–2770, https://doi.org/10.1002/cphc.201100346

[19] R.C. Deus, M. Cilense, C.R. Foschini, M.A. Ramirez, E. Longo, A.Z. Simões, Influence of mineralizer agents on the growth of crystalline CeO_2 nanospheres by the microwave-hydrothermal method, J. Alloy. Compd. 550 (2013) 245–251, https://doi.org/10.1016/j.jallcom.2012.10.001

[20] R.C. Deus, C.R. Foschini, B. Spitova, F. Moura, E. Longo, A.Z. Simões, Effect of soaking time on the photoluminescence properties of cerium oxide nanoparticles, Ceram. Int. 40 (2014) 1–9, https://doi.org/10.1016/j.ceramint.2013.06.043

[21] R.C. Deus, J.A. Cortés, M.A. Ramirez, M.A. Ponce, J. Andres, L.S.R. Rocha, E. Longo, A.Z. Simões, Photoluminescence properties of cerium oxide nanoparticles as a function of lanthanum content, Mater. Res. Bull. 70 (2015) 416–423, https://doi.org/10.1016/j.materresbull.2015.05.006

[22] R. Cristina de Oliveira, L. Cabral, A.C. Cabral, P.B. Almeida, N. Tibaldi, J.R. Sambrano, A.Z. Simões, C.E. Macchi, F. Moura, G.E. Marques, M.A. Ponce, E. Longo, Charge transfer in Pr-Doped cerium oxide: experimental and theoretical investigations, Mater. Chem. Phys. 249 (2020) 122967, https://doi.org/10.1016/j.matchemphys.2020.122967

[23] L.S.R. Rocha, F. Schipani, C.M. Aldao, L. Cabral, A.Z. Simoes, C. Macchi, G.E. Marques, M.A. Ponce, E. Longo, Experimental and ab Initio studies of deep-bulk traps in doped rare-earth oxide thick films, J. Phys. Chem. C (2019), https://doi.org/10.1021/acs.jpcc.9b07217

[24] L.S.R. Rocha, M. Cilense, M.A. Ponce, C.M. Aldao, L.L. Oliveira, E. Longo, A.Z. Simoes, Novel gas sensor with dual response under CO(g) exposure: optical and electrical stimuli, Phys. B Condens. Matter 536 (2018) 280–288, https://doi.org/10.1016/j.physb.2017.10.083

[25] P.P. Ortega, L.S.R. Rocha, J.A. Cortés, M.A. Ramirez, C. Buono, M.A. Ponce, A.Z. Simões, Towards carbon monoxide sensors based on europium doped cerium dioxide, Appl. Surf. Sci. 464 (2019) 692–699, https://doi.org/10.1016/j.apsusc.2018.09.142

[26] A.C. Cabral, L.S. Cavalcante, R.C. Deus, E. Longo, A.Z. Simões, F. Moura, Photoluminescence properties of praseodymium doped cerium oxide nanocrystals, Ceram. Int. 40 (2014) 4445–4453, https://doi.org/10.1016/j.ceramint.2013.08.117

[27] L.L. Oliveira, J.A. Cortés, B.S. Caldeira, T. Strusch, U. Wiedwald, A.Z. Simoes, Effects of dietary crude glycerin concentration on testicular morphology and oxidative stress markers and on plasma testosterone concentrations, J. Comp. Pathol. 185 (2021) 72–81, https://doi.org/10.1016/j.ceramint.2021.04.133

[28] P. Li, B. Wang, C. Qin, C. Han, L. Sun, Y. Wang, Band-gap-tunable CeO_2 nanoparticles for room-temperature NH_3 gas sensors, Ceram. Int. 46 (2020) 19232–19240, https://doi.org/10.1016/j.ceramint.2020.04.261

[29] S. Hussain, N. Aslam, X.Y. Yang, M.S. Javed, Z. Xu, M. Wang, G. Liu, G. Qiao, Unique polyhedron CeO_2 nanostructures for superior formaldehyde gas-sensing performances, Ceram. Int. 44 (2018) 19624–19630, https://doi.org/10.1016/j.ceramint.2018.07.212

[30] Q. Hu, B. Huang, Y. Li, S. Zhang, Y. Zhang, X. Hua, G. Liu, B. Li, J. Zhou, E. Xie, Z. Zhang, Methanol gas detection of electrospun CeO_2 nanofibers by regulating Ce^{3+}/Ce^{4+} mole ratio via Pd doping, Sens. Actuators B: Chem. 307 (2020) 127638, https://doi.org/10.1016/j.snb.2019.127638

[31] N. Izu, W. Shin, N. Murayama, S. Kanzaki, Resistive oxygen gas sensors based on CeO_2 fine powder prepared using mist pyrolysis, Sens. Actuators, B Chem. 87 (2002) 95–98, https://doi.org/10.1016/S0925-4005(02)00224-1

[32] A. Mirzaei, G. Neri, Microwave-assisted synthesis of metal oxide nanostructures for gas sensing application: a review, Sens. Actuators, B Chem. 237 (2016) 749–775, https://doi.org/10.1016/j.snb.2016.06.114

[33] B. Soni, S. Makkar, S. Biswas, Defects induced tailored optical and magnetic properties of Zn-doped CeO_2 nanoparticles synthesized by a facile sol-gel type process, J. Alloy. Compd. 879 (2021) 160149, https://doi.org/10.1016/j.jallcom.2021.160149

[34] M. Ramachandran, R. Subadevi, M. Sivakumar, Role of pH on synthesis and characterization of cerium oxide (CeO_2) nano particles by modified co-precipitation method, Vacuum 161 (2019) 220–224, https://doi.org/10.1016/j.vacuum.2018.12.002

[35] A.A.G. Santiago, N.F. Andrade Neto, E. Longo, C.A. Paskocimas, F.V. Motta, M.R.D. Bomio, Fast and continuous obtaining of Eu^{3+} doped CeO_2 microspheres by ultrasonic spray pyrolysis: characterization and photocatalytic activity, J. Mater. Sci. Mater. Electron. 30 (2019) 11508–11519, https://doi.org/10.1007/s10854-019-01506-7

[36] M. Nyoka, Y.E. Choonara, P. Kumar, P.P.D. Kondiah, V. Pillay, Synthesis of cerium oxide nanoparticles using various methods: Implications for biomedical applications, Nanomaterials 10 (2020) 242, https://doi.org/10.3390/nano10020242

[37] R.C. de Oliveira, R.A.C. Amoresi, N.L. Marana, M.A. Zaghete, M. Ponce, A.J. Chiquito, J.R. Sambrano, E. Longo, A.Z. Simões, Influence of synthesis time on the morphology and properties of CeO_2 nanoparticles: an experimental–theoretical study, Cryst. Growth Des. 20 (2020) 5031–5042, https://doi.org/10.1021/acs.cgd.0c00165

[38] S.A.M.K. Ansari, E. Ficiarà, F.A. Ruffinatti, I. Stura, M. Argenziano, O. Abollino, R. Cavalli, C. Guiot, F. D'Agata, Magnetic iron oxide nanoparticles: synthesis, characterization and functionalization for biomedical applications in the central nervous system, Materials Vol. 12 (2019) 465, https://doi.org/10.3390/MA12030465

[39] R. Shegokar, M. Nakach, Large-scale manufacturing of nanoparticles—an industrial outlook, Drug Deliv. Asp. (2020) 57–77, https://doi.org/10.1016/B978-0-12-821222-6.00004-X

[40] A.A. Coelho, TOPAS and TOPAS-Academic: An optimization program integrating computer algebra and crystallographic objects written in C++: an, J. Appl. Crystallogr 51 (2018) 210–218, https://doi.org/10.1107/S1600576718000183

[41] H.M. Rietveld, A profile refinement method for nuclear and magnetic structures, J. Appl. Crystallogr. 2 (1969) 65–71, https://doi.org/10.1107/s0021889869006558

[42] P. Makuła, M. Pacia, W. Macyk, How to correctly determine the band gap energy of modified semiconductor photocatalysts based on UV-vis spectra, J. Phys. Chem. Lett. 9 (2018) 6814–6817, https://doi.org/10.1021/acs.jpclett.8b02892

[43] N. Tibaldi, M.A. Ponce, P. Kalafatovich, H. Asencio, M.P. Desimone, A.Z. Simões, L. S.R. Rocha, E. Longo, A Device for the Optoelectronic Characterization of Materials, 20150103953, 2015.

[44] N. Tibaldi, M.A. Ponce, P. Kalafatovich, H. Asencio, M.P. Desimone, A.Z. Simões, L. S.R. Rocha, E. Longo, A Device for the Optoelectronic Characterization of Materials, BR 10 2016 028383 3, 2016.

[45] R.D. Shannon, Revised effective ionic radii and systematic studies of interatomic distances in halides and chalcogenides, Acta Crystallogr. Sect. A 32 (1976) 751–767, https://doi.org/10.1107/S0567739476001551

[46] D. He, H. Hao, D. Chen, J. Liu, J. Yu, J. Lu, F. Liu, G. Wan, S. He, Y. Luo, Synthesis and application of rare-earth elements (Gd, Sm, and Nd) doped ceria-based solid solutions for methyl mercaptan catalytic decomposition, Catal. Today 281 (2017) 559–565, https://doi.org/10.1016/j.cattod.2016.06.022

[47] M. Jamshidijam, P. Thangaraj, A. Akbari-Fakhrabadi, M.A. Niño Galeano, J. Usuba, M.R. Viswanathan, Influence of rare earth (RE=Nd, Y, Pr and Er) doping on the microstructural and optical properties of ceria nanostructures, Ceram. Int. 43 (2017) 5216–5222, https://doi.org/10.1016/j.ceramint.2017.01.046

[48] S. Tiwari, G. Rathore, N. Patra, A.K. Yadav, D. Bhattacharya, S.N. Jha, C.M. Tseng, S.W. Liu, S. Biring, S. Sen, Oxygen and cerium defects mediated changes in structural, optical and photoluminescence properties of Ni substituted CeO_2, J. Alloy. Compd. 782 (2019) 689–698, https://doi.org/10.1016/j.jallcom.2018.12.009

[49] F. Dong, Y. Meng, W. Han, H. Zhao, Z. Tang, Morphology effects on surface chemical properties and lattice defects of Cu/CeO_2 catalysts applied for low-temperature CO oxidation, Sci. Rep. 9 (2019) 1–14, https://doi.org/10.1038/s41598-019-48606-2

[50] S.A. Acharya, V.M. Gaikwad, S.W. D'Souza, S.R. Barman, Gd/Sm dopant-modified oxidation state and defect generation in nano-ceria, Solid State Ion. 260 (2014) 21–29, https://doi.org/10.1016/j.ssi.2014.03.008

[51] S.K. Alla, E.V. Prasadarao Komarala, R.K. Mandal, N.K. Prasad, Structural, optical and magnetic properties of Cr-substituted CeO_2 nanoparticles, Mater. Chem. Phys. 182 (2016) 280–286, https://doi.org/10.1016/j.matchemphys.2016.07.033

[52] N. Kainbayev, M. Sriubas, D. Virbukas, Z. Rutkuniene, K. Bockute, S. Bolegenova, G. Laukaitis, Raman study of nanocrystalline-doped ceria oxide thin films, Coatings 10 (2020) 432, https://doi.org/10.3390/coatings10050432

[53] Y.H. Quan, C. Miao, T. Li, N. Wang, M.M. Wu, N. Zhang, J.X. Zhao, J. Ren, Effect of preparation methods on the structure and catalytic performance of CeO_2 for toluene combustion, Ranliao Huaxue Xuebao/J. Fuel Chem. Technol. 49 (2021) 211–219, https://doi.org/10.1016/S1872-5813(21)60014-2

[54] L.S.R. Rocha, R.A.C. Amoresi, H. Moreno, M.A. Ramirez, M.A. Ponce, C.R. Foschini, E. Longo, A.Z. Simões, Novel approaches of nanoceria with magnetic, photo-luminescent, and gas-sensing properties, 2020. ⟨https://doi.org/10.1021/ac-somega.9b04250⟩.

[55] L. Yan, R. Yu, J. Chen, X. Xing, Template-free hydrothermal synthesis of CeO$_2$ nano-octahedrons and nanorods: Investigation of the morphology evolution, Cryst. Growth Des. 8 (2008) 1474–1477, https://doi.org/10.1021/cg800117v

[56] H.X. Mai, L.D. Sun, Y.W. Zhang, R. Si, W. Feng, H.P. Zhang, H.C. Liu, C.H. Yan, Shape-selective synthesis and oxygen storage behavior of ceria nanopolyhedra, nanorods, and nanocubes, J. Phys. Chem. B. 109 (2005) 24380–24385, https://doi.org/10.1021/jp055584b

[57] G. Spezzati, A.D. Benavidez, A.T. DeLaRiva, Y. Su, J.P. Hofmann, S. Asahina, E.J. Olivier, J.H. Neethling, J.T. Miller, A.K. Datye, E.J.M. Hensen, CO oxidation by Pd supported on CeO$_2$(100) and CeO$_2$(111) facets, Appl. Catal. B Environ. 243 (2019) 36–46, https://doi.org/10.1016/j.apcatb.2018.10.015

[58] Y. Ma, P. Ou, Z. Wang, A. Zhu, L. Lu, Y. Zhang, W. Zeng, J. Song, J. Pan, Interface engineering in CeO$_2$ (1 1 1) facets decorated with CdSe quantum dots for pho-tocatalytic hydrogen evolution, J. Colloid Interface Sci. 579 (2020) 707–713, https://doi.org/10.1016/j.jcis.2020.06.100

[59] C.C. Hwang, T.H. Huang, J.S. Tsai, C.S. Lin, C.H. Peng, Combustion synthesis of nanocrystalline ceria (CeO$_2$) powders by a dry route, Mater. Sci. Eng. B Solid-State Mater. Adv. Technol. 132 (2006) 229–238, https://doi.org/10.1016/j.mseb.2006.01.021

[60] Y.P. Fu, C.H. Lin, C.S. Hsu, Preparation of ultrafine CeO$_2$ powders by microwave-induced combustion and precipitation, J. Alloy. Compd. 391 (2005) 110–114, https://doi.org/10.1016/j.jallcom.2004.07.079

[61] S. Lu, F. Wang, C. Chen, F. Huang, K. Li, Catalytic oxidation of formaldehyde over CeO$_2$-Co$_3$O$_4$ catalysts, J. Rare Earths 35 (2017) 867–874, https://doi.org/10.1016/S1002-0721(17)60988-8

[62] R. Srivastava, Eco-friendly and morphologically-controlled synthesis of porous CeO$_2$ microstructure and its application in water purification, J. Colloid Interface Sci. 348 (2010) 600–607, https://doi.org/10.1016/j.jcis.2010.04.076

[63] M. Mousavi-Kamazani, F. Azizi, Facile sonochemical synthesis of Cu doped CeO$_2$ nanostructures as a novel dual-functional photocatalytic adsorbent, Ultrason. Sonochem. 58 (2019) 104695, https://doi.org/10.1016/j.ultsonch.2019.104695

[64] J. Malleshappa, H. Nagabhushana, B.D. Prasad, S.C. Sharma, Y.S. Vidya, K.S. Anantharaju, Structural, photoluminescence and thermoluminescence properties of CeO$_2$ nanoparticles, Optik (Stuttg) 127 (2016) 855–861, https://doi.org/10.1016/j.ijleo.2015.10.114

[65] G. Wang, Q. Mu, T. Chen, Y. Wang, Synthesis, characterization and photo-luminescence of CeO$_2$ nanoparticles by a facile method at room temperature, J. Alloy. Compd. 493 (2010) 202–207, https://doi.org/10.1016/j.jallcom.2009.12.053

[66] K.Y. Jung, J.C. Lee, D.S. Kim, B.K. Choi, W.J. Kang, Co-doping effect of mono-valent alkali metals on optical properties of CeO$_2$:Eu nanophosphor prepared by spray pyrolysis and application for preparing pearlescent pigments with red emission, J. Lumin. 192 (2017) 1313–1321, https://doi.org/10.1016/j.jlumin.2017.09.017

[67] A.K.V. Raj, P.P. Rao, T.S. Sreena, T.R.A. Thara, Influence of local structure on photoluminescence properties of Eu^{3+} doped CeO$_2$ red phosphors through in-duced oxygen vacancies by contrasting rare earth substitutions, Phys. Chem. Chem. Phys. 19 (2017) 20110–20120, https://doi.org/10.1039/c7cp02741a

[68] K. Binnemans, Interpretation of europium(III) spectra, Coord. Chem. Rev. 295 (2015) 1–45, https://doi.org/10.1016/j.ccr.2015.02.015

[69] X. Liu, S. Chen, X. Wang, Synthesis and photoluminescence of CeO$_2$:Eu^{3+} phos-phor powders, J. Lumin. 127 (2007) 650–654, https://doi.org/10.1016/j.jlumin.2007.03.014

[70] G. Vimal, K.P. Mani, P.R. Biju, C. Joseph, N.V. Unnikrishnan, M.A. Ittyachen, Structural studies and luminescence properties of CeO$_2$:Eu^{3+} nanophosphors synthesized by oxalate precursor method, Appl. Nanosci. 5 (2015) 837–846, https://doi.org/10.1007/s13204-014-0375-5

[71] L. Li, H.K. Yang, B.K. Moon, Z. Fu, C. Guo, J.H. Jeong, S.S. Yi, K. Jang, H.S. Lee, Photoluminescence properties of CeO$_2$:Eu^{3+} nanoparticles synthesized by a sol-gel method, J. Phys. Chem. C 113 (2009) 610–617, https://doi.org/10.1021/jp808688w

[72] G. Han, G. Wang, D. Li, J. Bai, G. Diao, Novel upconversion Er, Yb-CeO$_2$ hollow spheres as scattering layer materials for efficient dye-sensitized solar cells, Sol. Energy Mater. Sol. Cells 160 (2017) 54–59, https://doi.org/10.1016/j.solmat.2016.10.021

[73] C.Y. Chen, K.H. Chang, H.Y. Chiang, S.J. Shih, Preparation of a porous ceria coating for a resistive oxygen sensor, Sens. Actuators, B Chem. 204 (2014) 31–41, https://doi.org/10.1016/j.snb.2014.07.053

[74] Y. Makinose, T. Taniguchi, K.I. Katsumata, K. Okada, N. Matsushita, Facet control of ceria nanocrystals synthesized by an oleate-modified hydrothermal method, Adv. Powder Technol. 27 (2016) 64–71, https://doi.org/10.1016/j.apt.2015.10.004

[75] C.M. Aldao, F. Schipani, M.A. Ponce, E. Joanni, F.J. Williams, Conductivity in SnO$_2$ polycrystalline thick film gas sensors: Tunneling electron transport and oxygen diffusion, Sens. Actuators, B Chem. 193 (2014) 428–433, https://doi.org/10.1016/j.snb.2013.11.114

[76] H.L. Tuller, A.S. Nowick, Small polaron electron transport in reduced CeO$_2$ single crystals, J. Phys. Chem. Solids 38 (1977) 859–867, https://doi.org/10.1016/0022-3697(77)90124-X

[77] T. Hayashi, Y. Tokura, A. Fujiwara, Field-dependent hopping conduction, Phys. B Condens. Matter 541 (2018) 19–23, https://doi.org/10.1016/j.physb.2018.04.019

[78] D. Du, J. Kullgren, K. Hermansson, P. Broqvist, From ceria clusters to nano-particles: superoxides and supercharging, J. Phys. Chem. C. 123 (2019) 1742–1750, https://doi.org/10.1021/acs.jpcc.8b08977

[79] G.V.S. Rao, S. Ramdas, P.N. Mehrotra, C.N.R. Rao, Electrical transport in rare-earth oxides, J. Solid State Chem. 2 (1970) 377–384, https://doi.org/10.1016/0022-4596(70)90095-2

[80] S.M.A. Durrani, M.F. Al-Kuhaili, I.A. Bakhtiari, Carbon monoxide gas-sensing properties of electron-beam deposited cerium oxide thin films, Sens. Actuators, B Chem. 134 (2008) 934–939, https://doi.org/10.1016/j.snb.2008.06.049

[81] N. Izu, S. Nishizaki, T. Itoh, M. Nishibori, W. Shin, I. Matsubara, Gas response, response time and selectivity of a resistive CO sensor based on two connected CeO$_2$ thick films with various particle sizes, Sens. Actuators, B Chem. 136 (2009) 364–370, https://doi.org/10.1016/j.snb.2008.12.018

[82] N. Izu, I. Matsubara, T. Itoh, T. Akamatsu, W. Shin, CO responses of sensors based on cerium oxide thick films prepared from clustered spherical nanoparticles, Sens. (Switz.) 13 (2013) 3252–3261, https://doi.org/10.3390/s130303252

[83] E.R. López-Mena, C.R. Michel, A.H. Martínez-Preciado, A. Elías-Zúñiga, Simple route to obtain nanostructured CeO$_2$ microspheres and CO gas sensing performance, Nanoscale Res. Lett. 12 (2017) 1–10, https://doi.org/10.1186/s11671-017-1951-x